



Iron Silicide Formation from Fe Thin-Film Electrodeposition on Hydrogen-Terminated Si(111)

J. Zarpellon, H. F. Jurca, J. J. Klein, W. H. Schreiner,
N. Mattoso, and D. H. Mosca^{*,z}

Departamento de Física, Universidade Federal do Paraná, 81531-990 Curitiba PR, Brasil

We report on the surface morphology, crystalline, and electronic properties of Fe thin films potentiostatically electrodeposited on hydrogen-terminated Si(111) substrates. Spontaneous reaction between Fe deposits and hydrogen-terminated Si surfaces have been observed at room temperature with formation of polycrystalline silicides Fe₂Si and Fe₅Si₃, together with metallic Fe having a body-centered cubic structure. X-ray photoemission spectroscopy and X-ray diffraction measurements have been performed to investigate the thermal stability between Fe and Si under high-vacuum thermal treatments up to 300°C.
© 2005 The Electrochemical Society. [DOI: 10.1149/1.2097607] All rights reserved.

Manuscript submitted January 3, 2005; revised manuscript received July 12, 2005. Available electronically October 18, 2005.

Metal deposition on semiconductor surfaces has been extensively investigated primarily because of the technological importance of Schottky contacts. Notably, the direct metal deposition onto Si is of interest to the microelectronics industry, for example, to improve interconnects in ultralarge-scale integration metallization,¹ and to build Schottky diodes.^{2,3} The integration of magnetic materials and nanostructures with semiconductor electronics is an increasingly interesting approach to explore spin injection from metal/semiconductor interfaces⁴ for a new generation of electronic technology.⁵ In spite of this, surprisingly little work has been done on direct electrochemical deposition of ferromagnetic materials on Si surfaces, e.g., Co⁶ and Ni⁷ nanoclusters, Co films,⁸⁻¹⁰ Ni,^{11,12} NiCu alloys films,¹³ Co–Ni–Cu/Cu multilayers,^{14,15} NiFe Permalloy films,^{15,16} and Fe on porous Si.^{17,18} In this work, we investigated the specific case of Fe deposition on hydrogen-terminated n-type Si(111) surfaces and our attention was focused on the morphology as well as the crystalline and electronic structures of the Fe deposits.

Experimental

Fe deposits were potentiostatically deposited from aqueous acidic solutions containing 10 mM Fe(NH₄)₂(SO₄)₂ chemical grade directly on n-type Si(111) wafers with resistivity of 50–80 Ω cm. All electrochemical experiments were performed with a commercial galvanostat/potentiostat (EG&G model 273A) using a conventional cell with three stationary electrodes. A platinum disk was used as counter electrode, whereas an Ag/AgCl reference electrode was employed. Rectangular slices of Si wafers with area of 2.8 cm² were used as working electrodes after removal of the native oxide by chemical HF-etching prior to electrodeposition experiments. The HF-etching is known to lead to hydrogen-terminated Si(111) surfaces rather stable to oxygen exposure at room temperature.¹⁹ Gallium-aluminum alloying was used on the rear of the Si wafers to form a good ohmic contact. The pH was kept at 2.5 by addition of an appropriate amount of H₂SO₄. All potentials of this work are given with respect to the Ag/AgCl reference electrode. Samples grown from 10-mM Fe(NH₄)₂(SO₄)₂ solutions at cathodic potential of –1.2 V for 10 min give rise to homogeneous Fe deposits which are adherent with metallic shine and low conductivity. These deposits become grayish with an insulating character when stored under atmospheric conditions.

X-ray diffraction (XRD) analyses were performed in the conventional Bragg-Brentano geometry using Co Kα radiation to avoid fluorescence. X-ray photoelectron spectroscopy (XPS) measurements were carried out using a commercial VG ESCA3000 system with a base pressure of 3 × 10^{–8} Pa, while XPS profiles were obtained by sputtering with Ar⁺ ions (3 keV, 5 μA). A previous calibration of the sputtering rate for pure iron films gives approxi-

mately 10 nm/h. The spectra were collected using Mg Kα radiation and the overall energy resolution was approximately 0.8 eV. Atomic force microscopy (AFM) were performed using a scanning probe microscope (Shimadzu SPM-9500J3) operating in the contact mode.

Results and Discussion

Figure 1 shows a typical CV obtained at a sweep potential rate of 10 mV/s in the solution containing 10 mM Fe(NH₄)₂(SO₄)₂ onto hydrogen-terminated Si(111) surface. The potential scan in the cathodic direction reveals that the reduction of the Fe²⁺ ions has onset potential at –1.05 V, leading to a Fe nucleation wave. Superimposed on the reduction wave is seen a rapid increase of the cathodic current due to hydrogen evolution. We believe that the spread of reduction potential between –1.05 and –1.30 V associated with Fe deposition is related to a charge-transfer layer with complexed and solvated Fe ions as well as different activated sites for nucleation at the silicon surface. Evidence of a complex mechanism in the charge exchange processes appears when the potential scan is performed in the anodic direction.

For the potential scan in the anodic direction, the nucleation cycle starting from the potential scan in the cathodic direction finishes at around –1.0 V after a strong hydrogen evolution. At the end of the voltammogram, i.e., potential region of –1.0–0.0 V, two peaks of anodic current are observed. Even if it is plausible that the anodic oxidation of Si could occur at these potentials,^{17,20} the two anodic peaks are likely the oxidation of Fe to Fe²⁺ and Fe²⁺ to Fe³⁺ (or Fe to Fe³⁺ in some part), as indicated by XRD measurements of specimens (not shown) prepared at these anodic currents. A simple visual inspection clearly confirms that anodic peaks promote the dissolution of Fe deposits by exposing bare Si surface. Charge exchange processes with coupling between the anodic dissolution of silicon and cathodic metal deposition from the metallic ion solutions have been recently discussed.²⁰ However, a fluoride solution has been used and therefore the discussion cannot simply apply to our present experiments. The time evolution of the cathodic current for potentiostatic deposition at –1.2 V is shown in the inset of Fig. 1. After the initial transient, the current decreases and then reaches a stationary value associated with diffusion limit. Certainly, the stationary current coincides with the maximum rate of (solvated and complexed) ions arriving at the surface layer, and current transient strongly depends on the applied overpotential between electrodes of the cell and the ion concentration in the electrolyte. As we discuss below, the initial growth seems to occur by random nucleation with an interfacial silicide formation assisted by diffusion-limited aggregation of the ions.²¹

We can only speculate how the iron deposition could occur through the displacement of surface hydrogen atoms which terminate the Si(111) surface. Calculations using Nerst equations for the splitting of Si–H bonds at pH 2 and 25°C by assuming that the dislocation of the equilibrium balance arises only from the increase of the H⁺ active ions results in the reaction ≡Si–H →

* Electrochemical Society Active Member.

^z E-mail: mosca@fisica.ufpr.br

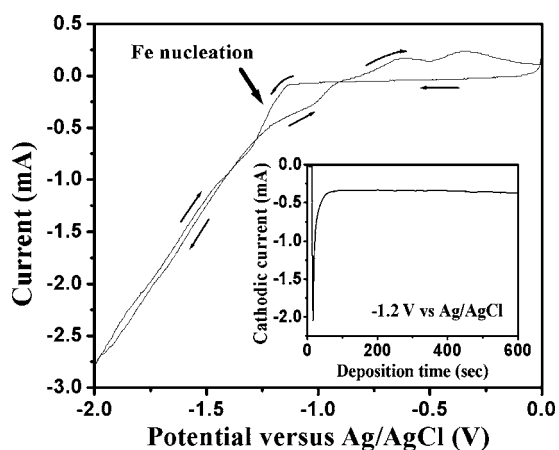


Figure 1. Cyclic voltammogram obtained from 10-mM $\text{Fe}(\text{NH}_4)_2(\text{SO}_4)_2$ solution. The inset shows a plot of the current as a function of deposition time.

$\equiv \text{Si}^*$ (active) + H^+ + e^- is -1.1 V at pH 2 and 25°C .^{12,22} Our experiments were performed under potential -1.2 V vs saturated Ag/AgCl, i.e., -1.42 V vs a normal hydrogen reference electrode (NHE). Although the mechanism of the chemical deposition and compound formation is certainly more complex and involves various other factors, the above estimated potential value indicates that iron deposition by galvanic displacement between Fe^{2+} and $\equiv \text{Si}-\text{H}$ is thermodynamically feasible in our experiments. It is worthy of note that a narrow electrochemical window was found for homogeneous and metallic Fe deposition. In our experiments, nonhomogeneous and insulating deposits are found when solutions with concentrations smaller than 10 mM $\text{Fe}(\text{NH}_4)_2(\text{SO}_4)_2$ or pH values higher than 3.2 are used. We have used the ammonium sulfate trying to increase the Fe ion discharging ability, but it does not eliminate the hydroxide formation as shown below. In addition, the formation of more homogeneous coatings was obtained by illumination of the silicon electrolyte junctions.

The surface morphology was determined by AFM analysis. Figure 2a and b exhibits AFM images of Fe electrodeposits grown on Si(111) surfaces after 5 and 10 min of Fe deposition from 10-mM $\text{Fe}(\text{NH}_4)_2(\text{SO}_4)_2$ solution under cathodic potential of -1.2 V. Fe electrodeposits onto Si(111) surfaces exhibit a surface morphology having submicrometer grains with slightly flat terraces. This microstructure is a possible reason for the brightness of these deposits. Such a surface morphology is not surprising, because the nucleation and growth of metals on semiconductor surfaces from liquids generally proceeds by the Volmer-Weber mechanism, i.e., three-dimensional growth of metal nuclei. In our case, the Si surface stability is promoted by hydrogen passivation; and thus even for Si(111) surfaces which are not coordinatively saturated, these surfaces tend to have a low surface energy, which favors a Volmer-Weber growth mode.²³

XRD was performed to determine the crystallographic structure and phase formation in the electrodeposits. XRD patterns (θ - 2θ scans) obtained for the freshly as-deposited sample and two different annealing temperatures of individual pieces of the same sample are shown in Fig. 3. In the plot the diffraction intensity is arbitrary, but all the XRD patterns were normalized with respect to the intensity of the Si(111) Bragg reflection positioned around $2\theta = 33.2^\circ$ (not shown), which was used to orient the samples, maximizing the diffracted intensity in the experiments. For higher annealing temperatures, significant amounts of iron oxyhydroxide (FeOOH), iron oxide (Fe_2O_3), and SiO_2 from the Si substrate are observed. These findings are not surprising because the oxidation is known to easily occur at polycrystalline Fe surfaces exposed to air. A fraction of these oxide phases does not show any significant changes under

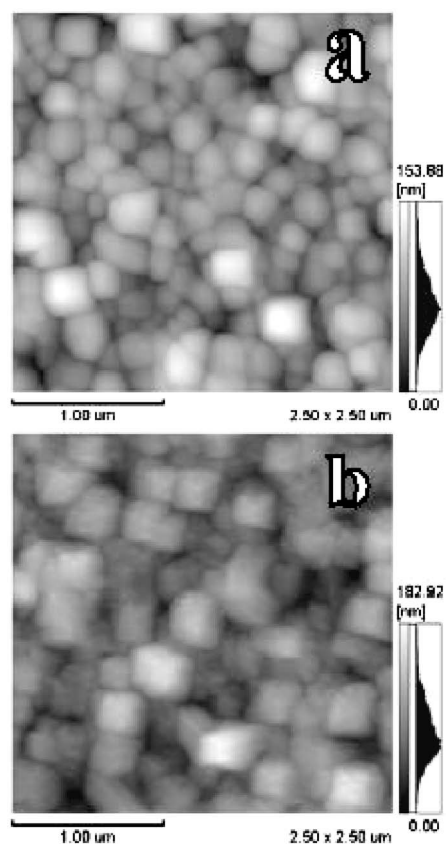


Figure 2. AFM images of Fe deposits on silicon surfaces obtained in contact mode. Fe deposit after (a) 5 and (b) 10 min of deposition from 10-mM $\text{Fe}(\text{NH}_4)_2(\text{SO}_4)_2$ solutions at cathodic potential of -1.2 V.

annealing and could be largely attributed to the high chemical activity of fresh iron surfaces under exposure to the atmosphere. The relative amount of oxygen along the film thickness was followed by XPS depth profiling analyses. Spontaneous formation of Fe-rich silicides (Fe_2Si and Fe_5Si_3) is also observed from XRD patterns. As in the bulk Fe-Si system, where a continuous range of solid solutions are formed, Fe-Si(111) interface has also revealed the formation of a large variety of Fe silicides. Bulk Si-rich silicide phases β - FeSi_2

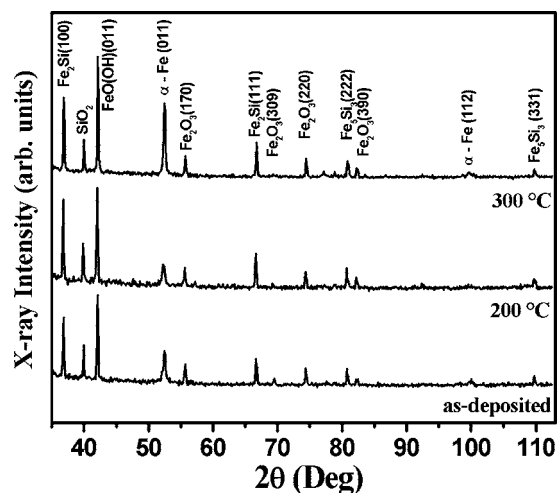


Figure 3. XRD patterns of Fe deposits. As-prepared and annealed samples are indicating alongside normalized diffractograms.

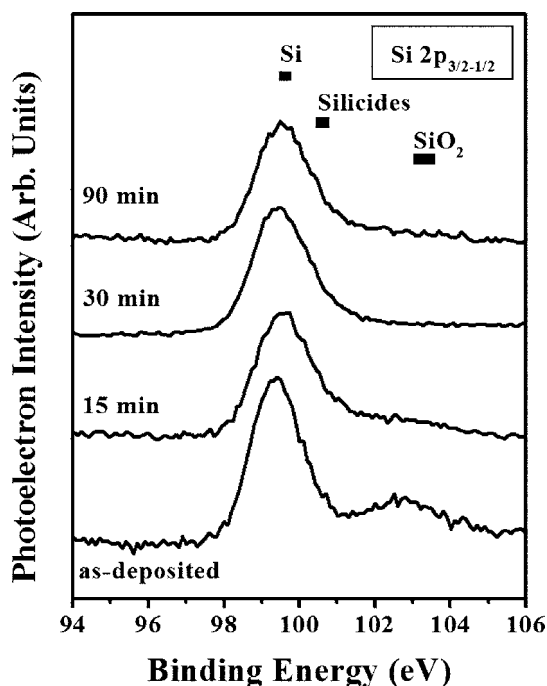


Figure 4. Si $2p_{3/2-1/2}$ core-level spectra of thin Fe deposits for some selected sputtering times as indicated. The dark bars drawn on the top of the panel correspond to the binding energy range for Si 2p photoelectrons for each compound type.²³

(orthorhombic structure) and ϵ -FeSi (B_{20} structure) as well as metastable $Fe(Si_{1-x}Fe_x)$ silicides ($1 < x < 0$) with a local cubic CsCl structure have been obtained by different techniques.^{24,25} $Fe(Si_{1-x}Fe_x)$ thin films on Si(111) are ferromagnetic at room temperature for x values ranging from 0.15 to 0.50, and their stoichiometries are found by introducing Fe vacancies in the CsCl-type lattice. The spontaneous formation of the Fe_2Si is well known, but the silicide Fe_5Si_3 ($x = 0.25$) formation at room temperature is not expected. Nevertheless, the XRD of our films reveals the formation of this silicide phase with no significant changes from freshly as-deposited samples to annealed ones. The electrochemical activity is the agent responsible for the stability of Fe-rich silicide at the interface between Fe and Si. The electrodeposition kinetics is, therefore, different from the thermodynamics of physical vapor deposition techniques. We believe that the large values of growth rate imposed by us through solution concentration and large overpotential privilege a random deposition with local surface diffusion to neighboring sites, which privilege metastable silicide formation. Whereas in a simple random deposition only metastable and nonstoichiometric silicides could be formed, our specific growth conditions lead to stoichiometric and thermally stable compounds.

XPS analyses indicate that all deposits do not contain impurities and exhibit an elemental composition consisting of Fe, Si, and O with a residual layer of N and C adsorbates. Figure 4 exhibits the depth evolution of the Si 2p core-level spectra for a freshly deposited Fe thin film. Because iron silicide bonding is based on the rehybridization of the Fe d bands with Si sp_3 bands, an appreciable asymmetry in the Si 2p and Fe 2p core-level photoemission spectra is expected. Oxygen has an electronegativity value approximately twice that of those values observed for iron and silicon, so it is expected that the Fe-Si bonds should account for a small chemical shift toward higher binding energies with respect to bulk silicon. Thus, the Si 2p core-level spectra are decomposed into three components and backgrounds; i.e., pure Si component positioned at 99.5 eV binding energy, Si-O bond component centered at about 103 eV binding energy, and a component at around 100-eV binding

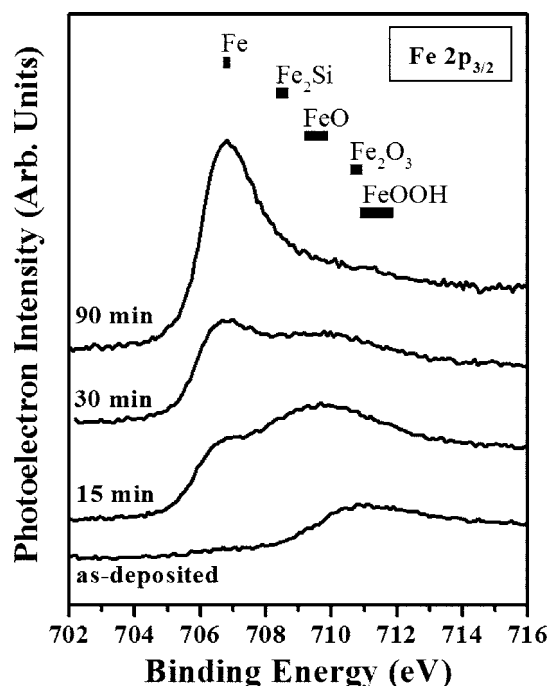


Figure 5. Fe $2p_{3/2}$ core-level spectra of Fe deposits for some selected sputtering times indicated alongside spectra. The dark bars drawn on the top of the panel correspond to the binding energy range for Fe 2p photoelectrons for each compound type.^{23,24}

energy which is correlated to Fe-Si bonds. The Si-O component drastically decreases as a function of the sputtering time, whereas the broadening of the pure Si component for higher binding energies indicates that a Si-Fe component is preserved and that silicides are predominantly localized close to the interface between Fe and Si.

Figure 5 shows the depth profiling of the Fe $2p_{3/2}$ core-level spectra for the same sample. Together with a metallic Fe component centered at around 706.8 eV binding energy, two other components peaking at around 710 and 713.5 eV binding energies are observed. The large energy shifts of these two extra components toward higher binding energies indicate that they are probably related to Fe oxide ($FeO-Fe_2O_3$) and oxyhydroxide ($FeOOH$) compounds.²⁶ The Fe silicides appear at slightly higher binding energy with respect to metallic Fe²⁵ and is buried in the spectra taken far from the Fe and Si interface. As a function of the depth, the Fe $2p_{3/2}$ photoemission spectra significantly change. Decomposition of spectra using a metallic Fe component and gaussian profiles for the oxide and oxyhydroxide components show that the integrated fraction corresponding to metallic Fe component increases from 10 to 42.9% after 30 min of argon-ion bombardment. Concomitantly, Fe-O components decrease from 71 to 48.9% and the Fe-oxyhydroxide component diminishes from 20 to 8.2% for the same sputter time. This clearly indicates that Fe oxyhydroxide is a superficial layer resulting from the moist air exposure after electrodeposition, whereas the Fe oxide is more intrinsically related to the deposition mechanism. Beyond this superficial oxygen-rich layer, metallic Fe and Fe silicide make a predominant contribution in the XPS spectra.

The depth profile of the Fe $2p_{3/2}$ and Si 2p photoemission spectra were also analyzed by decomposition of raw spectra in three components after a background subtraction. Figure 6 exhibits Si 2p and Fe $2p_{3/2}$ core-level spectra for an as-deposited sample collected after 90 min of argon ion bombardment, which results in a thin layer with photoelectron signals probing the interface between Fe and Si. According to Fig. 6a, a resulting pure silicon component is accompanied by a Si-Fe component centered at 100.2 eV binding energy (labeled as A in the spectra) and a small Si-O component (labeled as

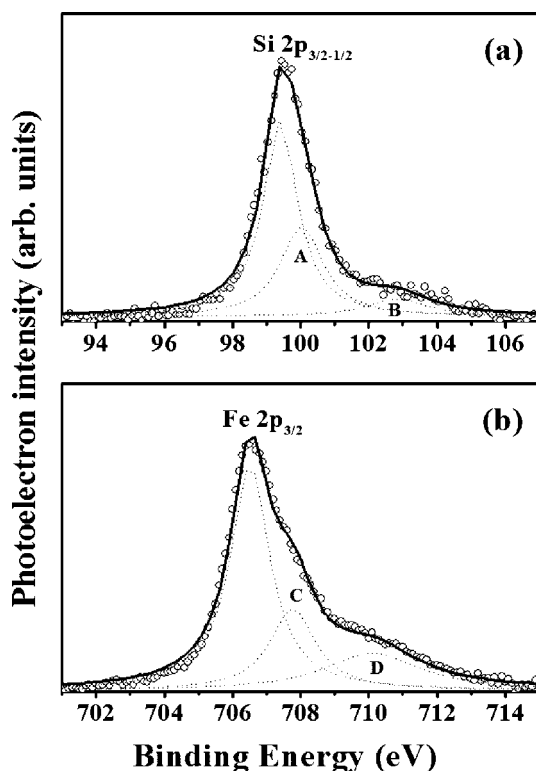


Figure 6. Si $2p_{3/2-1/2}$ and Fe $2p_{3/2}$ core-level spectra of as-prepared Fe deposits collected after 90 min of argon-ion bombardment. The solid curves are measured spectra and dotted lines are resolved components after background subtraction.

B in the spectra) centered at 103.3 eV binding energy. Concomitantly, a pronounced metallic Fe component at ~ 707 eV binding energy remains superimposed to two extra components, one centered at 708 eV binding energy (labeled as C) and another centered at 710.2 eV (labeled as D). These two peak energies associated with components C and D are quite close to the values reported by Berling et al.²⁵ for silicides Fe_2Si and Fe_5Si_3 for X-ray absorption experiments. However, the FeO compound cannot be completely discarded for the component labeled as D. The Fe silicide contribution is not evidenced from the Fe 2p photoemission signal. In spite of a low-energy resolution in our experiments, we believe that Fe electrodeposition with Fe silicide intermediate compounds is demonstrated. The effect of the oxygen on the Fe deposition and Fe silicide formation is not completely clear in this work, but there is no evidence of their accumulation at the interface Fe/silicide as reported by Swart and Berning.²⁷ Our results are qualitatively in agreement with sputter depth profiles of the XPS oxygen signal shown by Ronkel et al.¹⁷ for porous silicon substrates, i.e., during Fe deposition process the sample is oxidized. It is worth noticing that the complete removal of the Si oxide layer with formation of a stable H-terminated Si(111) is less evident in the case of porous silicon instead of flat Si(111) surfaces. The oxygen concentration in our Fe deposits could be related to the statement that Fe oxide formation prevents any silicide formation.

The postgrowth temperature effect on the deposits has been investigated by depth profiles of the Si 2p and Fe $2p_{3/2}$ core-level spectra. The typical sequence of photoemission spectra as a function of depth for a sample annealed at 300°C for 3 h is shown in Fig. 7 and 8. The same decomposition procedure as described above was used. The examination of the depth evolution of the Si 2p core-level spectra shown in Fig. 7 revealed that while pure Si component remains between 39.5 and 38.1%, the Si–O component decreases from 47.3 to 34.7% and the Si–Fe component increases from 16.6 to

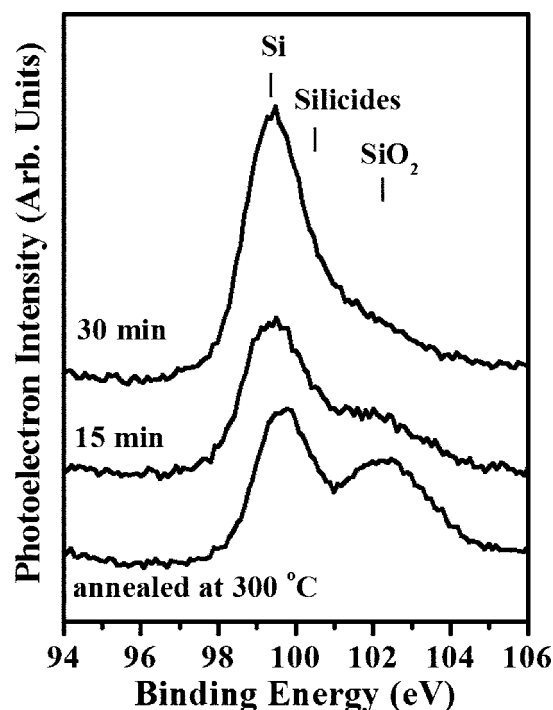


Figure 7. Si 2p core-level spectra of Fe deposits after annealing at 300°C during 3 h (bottom) and after sputter time given alongside spectra.

27.2% after 30 min of exposure to Ar-ion bombardment. A comparison between the integrated fraction of Si–Fe and Si–O components of the sample before and after annealing for equivalent sputter time of 30 min shows that the Si–Fe component remains practically constant at $\sim 27\%$, whereas the Si–O component, which is negligible before annealing, increases to 34.7%. Thus, the annealing effect does not significantly change the Fe silicide contribution but seems to indicate that oxygen atoms diffuse toward the interface between

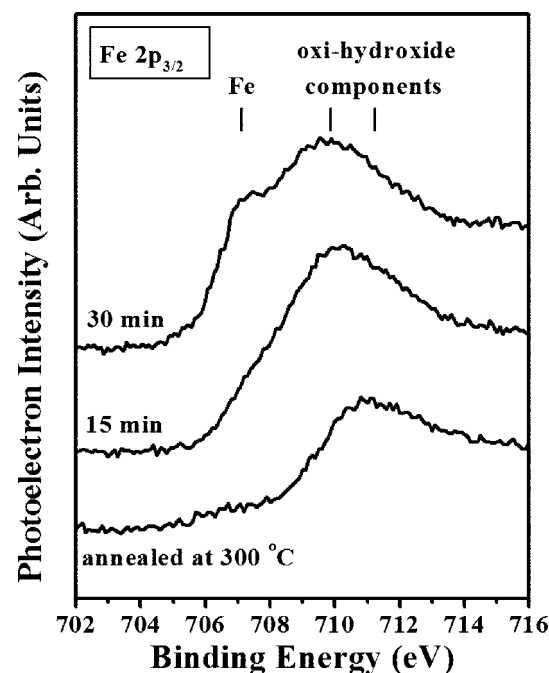


Figure 8. Fe $2p_{3/2}$ core-level spectra of Fe deposits after annealing at 300°C during 3 h (bottom) and after sputter times given alongside spectra.

Fe and Si. As pointed out previously, the Fe silicides formed at the interface are thermodynamically stable even if their oxygen environments have been enhanced. Analyses of the Fe 2p_{3/2} core-level spectra shown in Fig. 8 were also performed. For equivalent sputtering times of 30 min, the samples before and after annealing exhibit a reduction of the integrated area of the metallic Fe components of 42.9 and 37.2%, whereas the fraction of the Fe–O component increases from 48.9 to 60.8% and the FeOOH component decreases from 8.2 to 2.0%. We believe that these results corroborate to conclude that the increase of oxygen close to the Si interface is not an oxidation process of the sample coming from the residual base pressure of the quartz tube during annealing, but it could be understood as a dissociation of the Fe oxyhydroxide, which leads to the oxidation of the Fe together with the diffusion of oxygen atoms toward Si substrate.

Conclusion

In conclusion, we have shown that Fe deposition from aqueous sulfated solution onto hydrogen-terminated Si(111) surfaces could be obtained. An iron silicide-rich layer is formed at the interface between Fe and Si, which is buried below a metallic Fe-rich layer and covered by a layer consisting of iron oxide and oxyhydroxide. XRD measurements indicate the formation of polycrystalline Fe₂Si and Fe₃Si₃ phases concomitantly with the metallic Fe having a polycrystalline character with body-centered cubic structure. Fe silicide formation was confirmed by XPS analyses of the Fe 2p and Si 2p core-level photoemission signals. XPS experiments using depth profiles reveal that both metallic Fe and Fe silicide contributions increase as a function of depth after removal of a surface layer consisting of iron oxyhydroxides. Finally, post-growth thermal treatments indicate that Fe silicides are stable even if diffusion of oxygen atoms toward Si substrate occurs.

Acknowledgment

This work is partially financed by CNPq/PIBIC/UFPR and PRONEX/Fundação Araucária—CNPq.

Universidade Federal do Paraná assisted in meeting the publication costs of this article.

References

1. L. Santinacci, T. Djenizian, and P. Schmuki, *Appl. Phys. Lett.*, **79**, 1882 (2001).
2. G. Oskam, D. E. Van Heerden, and P. C. Searson, *Appl. Phys. Lett.*, **73**, 3241 (1998).
3. T. Zambelli, M. L. Munford, F. Pillier, M. C. Bernard, and P. Allongue, *J. Electrochem. Soc.*, **148**, C614 (2001).
4. S. Datta and B. Das, *Appl. Phys. Lett.*, **56**, 665 (1990).
5. S. A. Wolf, D. D. Awschalom, R. Buhrman, J. M. Daughton, S. von Molnár, M. L. Roukes, A. Y. Chtchelkanova, and D. M. Treger, *Science*, **294**, 1488 (2001).
6. M. V. Rastei, R. Meckenstock, J. Bucher, E. Devaux, and Th. Ebbsen, *Appl. Phys. Lett.*, **85**, 2050 (2004).
7. A. Imanishi, K. Morisawa, and Y. Nakato, *Electrochem. Solid-State Lett.*, **4**, C68 (2001).
8. M. L. Munford, M. L. Sartorelli, L. Seligman, and A. A. Pasa, *J. Electrochem. Soc.*, **149**, C274 (2002).
9. Y. Souche, J. P. Levy, E. Wagner, A. Lienard, L. Alvarez-Prado, and R. T. Collins, *J. Magn. Magn. Mater.*, **242**, 578 (2002).
10. M. L. Munford, L. Seligman, M. L. Sartorelli, E. Voltolini, L. F. O. Martins, W. Schwarzacher, and A. A. Pasa, *J. Magn. Magn. Mater.*, **226–230**, 1613 (2001).
11. P. Gorostiza, M. A. Kulandainathan, R. Diaz, F. Sanz, P. Allongue, and J. R. Morante, *J. Electrochem. Soc.*, **147**, 1026 (2000).
12. N. Takano, N. Hosoda, T. Yamada, and T. Osaka, *J. Electrochem. Soc.*, **146**, 1407 (1999).
13. R. G. Delattore, M. L. Sartorelli, A. Q. Schervenski, A. A. Pasa, and S. Guths, *J. Appl. Phys.*, **93**, 6154 (2003).
14. A. A. Pasa and W. Schwarzacher, *Phys. Status Solidi A*, **173**, 73 (1999).
15. A. P. O’Keeffe, O. I. Kasyutich, W. Schwarzacher, L. S. de Oliveira, and A. A. Pasa, *Appl. Phys. Lett.*, **73**, 1002 (1998).
16. L. G. Gao, P. Ma, K. M. Novogradez, and P. R. Norton, *J. Appl. Phys.*, **81**, 7595 (1997).
17. F. Ronkel, J. W. Schultze, and R. Arens-Fischer, *Thin Solid Films*, **276**, 40 (1996).
18. C. Renaux, V. Scheuren, and D. Flandre, *Microelectron. Reliab.*, **40**, 877 (2000).
19. X. Zhang, Y. J. Chabal, S. B. Christman, E. E. Chaban, and E. Garfunkel, *J. Vac. Sci. Technol. A*, **19**, 1725 (2001).
20. P. Gorostiza, M. A. Kulandainathan, R. Diaz, F. Sanz, P. Allongue, and J. R. Morante, *J. Electrochem. Soc.*, **147**, 1026 (2000).
21. B. Scharifker and G. Hills, *Electrochim. Acta*, **29**, 879 (1983).
22. P. Allongue, V. Costa-Kieling, and H. Gericher, *J. Electrochem. Soc.*, **140**, 1018 (1993).
23. A. Zangwill, *Physics at Surfaces*, Cambridge University Press, Cambridge, U.K. (1988).
24. U. Kafader, P. Wetzel, C. Pirri, and G. Gewinner, *Appl. Phys. Lett.*, **63**, 2360 (1993), and references therein.
25. D. Berling, G. Gewinner, M. C. Hanf, K. Hricovini, S. Hong, B. Loegel, A. Mehdaoui, C. Pirri, M. H. Tuilier, and P. Wetzel, *J. Magn. Magn. Mater.*, **191**, 331 (1999), and references therein.
26. *Handbook of X-Ray Photoemission Spectroscopy*, J. Chastain and R. C. King, Jr., Editors, Physics Electronics Div., Perkin-Elmer, Eden Prairie, MN (1995).
27. H. C. Swart and G. L. P. Berning, *Appl. Surf. Sci.*, **78**, 77 (1994).